International Journal of Applied Electromagnetics and Mechanics 34 (2010) 195–210
DOI 10.3233/JAE-2010-1311
IOS Press

Design of multi-DOF electromagnetic actuators using distributed multipole models and image method

Hungsun Son[a,*], Kun Bai[b], Jungyoul Lim[b] and Kok-Meng Lee[b]
[a]*Department of Mechanical and Aerospace Engineering, Nanyang Technological University, Singapore*
[b]*Department of Mechanical Engineering, Georgia Institute of Technology, Atlanta, GA, USA*

Abstract. Design and control of many electromagnetic actuators involve solving three dimensional (3D) magnetic fields of permanent magnets and/or electromagnets in the presence of magnetic conducting surfaces. This paper extends the distributed multipole (DMP) method, which offers compact but precise analysis for three dimensional magnetic fields in closed form, to account for the effects of magnetic conducting boundaries using the image method on the torque generated by electromagnetic actuators. We validate the proposed method referred to here as DMP-Image method by comparing the calculated torques against results computed by a finite element method (FEM). While two methods agree to within 5% in maximum torque, the DMP-image method takes less than 1% of the FEM computation time. Finally, we demonstrate the DMP-Image method to design a spherical motor in a class of multi-DOF actuators. While developed in the context of the multi-DOF actuators, the modeling methods presented in this paper are applicable to design of other PM-based actuators.

Keywords: Magnetic field, dipole, magnetic conducting boundary, image method, spherical motor

1. Introduction

Increasing demands for enhancing accuracy, high speed and flexibility of electromagnetic actuators can be found in numerous applications such as manufacturing, precision machining and robotics [1–3]. Most of the applications require orientation control of a tool and a workpiece. Recently, the growing interests in fuel-cell technology and low-cost electromechanical systems have motivated a number of researchers to develop compact and high efficient multi-DOF electromagnetic actuators. For the design and analysis of such novel electromechanical actuators, both accurate and fast computations of magnetic field distributions and force/torque analyses are often required.

Existing techniques for analyzing magnetic fields and designing multi-DOF PM-based actuators primarily rely on three approaches; namely, analytic solutions to Laplace's equation, numerical methods [4] and lumped-parameter analyses with some form of magnetic equivalent circuits (MEC) [5]. However, these existing approaches have difficulties in achieving both accuracy and low computation time simultaneously. In addition, many engineering problems with PMs or EMs are often required to solve the three dimensional (3D) magnetic fields with/without a magnetic conducting interface. These difficulties have led us to develop a new modeling method to derive closed-form field solutions for efficient design

*Corresponding author. Tel.: +65 6790 5508; Fax: +65 6792 4062; E-mail: hsson@ntu.edu.sg.

1383-5416/10/$27.50 © 2010 – IOS Press and the authors. All rights reserved

and accurate motion control of the actuators. Recently, distributed multi-pole (DMP) model has been developed using magnetic pole models in [6]. In this research, the DMP modelling method was used to characterize the magnetic field distribution in open space. Since the DMP method is here based on the concept of magnetic dipole and a limited set of known field information to construct a distributed dipole model, the method offers a relatively complete formulation for deriving the closed-form and an effective means to characterize the magnetic fields and torque computations for design and control of electromagnetic actuators. However, the method in [7] mainly focused on characterizing the magnetic field of a PM (or an EM) in free space. When the magnetic field is involving a magnetic conducting material, the field of the PM or EM interacts with the material boundary. The change of the field distribution results in the consequent change of the magnetic force and torque. To account for the effects of magnetic conducting materials on the DMP method, an image method can be applied along with the DMP modeling method.

As a basis problem-solving tool in electrostatics, the image method replaces the effects of the boundary on an applied field by adding and/or subtracting elementary fields behind the boundary line called image. For its simplicity but accuracy, the image method has been commonly used for analyzing boundary problems involving an eddy current in electromagnetic fields since the method provides certain solution forms for some important problems involving straight-line, circular and spherical boundaries in a simple manner, which decrease the need for formal solutions of Laplace's and Poisson's equations. The image method in [8] is used to analyze the unbounded magnetic field containing ferromagnetic materials by a numerical method (FEM). The magnetic field in two dimensional space to design a electromagnetic actuator are obtained in analytical forms using image and MEC methods [9]. Unlike the solutions in [9] with the first order accuracy, nonlinear approach is used to account for effects of eddy currents with magnetic conducting boundary [10]. However, the methods in [10] are mainly applicable for a simple structure of a conductive rod in a simplified geometry.

In this paper, we explore the image method with the DMP method to handle magnetic conducting boundaries. The methods (referred to here as DMP-Image) offer a relatively complete solution of the magnetic field involving magnetic conducting boundaries. Emphases are placed on spherical iron boundaries for three-DOF spherical motor design.

The remainder of this paper offers the following:

1. We formulate a class of spherical actuator problems with magnetic boundary conditions that appear to be difficult to satisfy if the governing Poisson's or Laplace's equation is to be solved directly. The conditions on the bounding surfaces in these problems are set up by appropriate image (equivalent) charges and solve using the image method.
2. To illustrate the DMP-Image, we model the magnetic field of a dipole (defined as a pair of source and sink with a well-defined separation) for three different boundaries; the dipole is (i) outside a grounded spherical rotor, (ii) inside a grounded hollow spherical stator, and (iii) in-between a pair of grounded spherical surfaces. With the field solutions from the DMP-Image, the torques can be calculated using one of the three methods; namely, the Lorentz force equation, Maxwell stress tensor, and force between magnetic charges.
3. We validate the DMP-Image method by comparing the calculated torques against results computed using FEM, which agree to within 5% in maximum torque. As will be shown, the DMP-Image method takes less than 1% of the FEM computation time. Finally, the effects of iron boundaries on the spherical motor were analyzed with the DMP-Image as an illustration of practical applications.

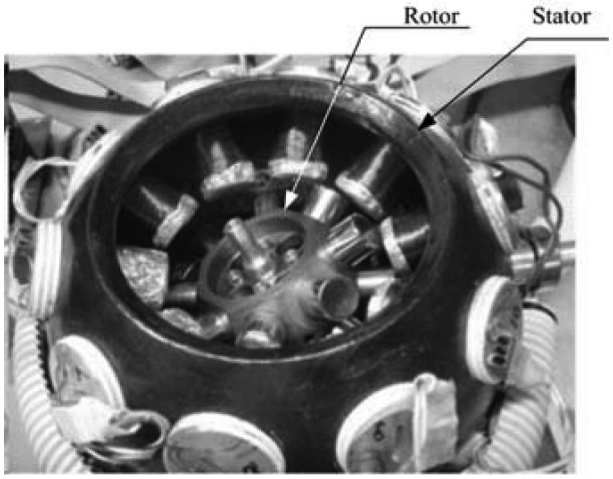

Fig. 1. Multi-DOF actuator (spheriacal wheel motor) [12].

2. Magnetic field of spherical grounded boundary

Figure 1 shows a multi-degree of freedom (DOF) electromagnetic actuator, called here as spherical wheel motor, which generates multi-degree of freedom motions in a single joint. The actuator mainly consists of three parts: a number of permanent magnets (PMs) in a rotor, electromagnets (EMs) in a stator with a certain pattern and a universal joint bearing at rotational centre of the rotor. The torque on the rotor is controlled by electric-current inputs through the EMs so as to control their orientation quickly, continuously, and isotropically in all directions.

Although these kinds of multi-DOF electromagnetic actuators have the similar designs, their structure materials are often different; magnetic materials (iron) and/or non-magnetic materials (aluminium) [7, 8]. In the paper, we investigate an effect of materials on the magnetic field generated by both PMs and EMs as well as the torque and performance of the electromagnetic actuators.

We consider here a class of electromagnetic problems where magnetic charges are in the presence of a magnetically grounded spherical boundary. Except at the point charges, the magnetic field is continuous and irrotational, for which a scalar potential Φ can then defined such that

$$\mathbf{H} = -\nabla\Phi \text{ and } \mathbf{B} = \mu_0\mathbf{H} \tag{1a,b}$$

where μ_0 is the permeability of free space. The formal approach for solving the magnetic field at every point outside the conducting boundary would be to solve the Laplace equation $\nabla^2\Phi = 0$ with the following boundary conditions: at points very close to the magnetic charge (source or sink), the potential Φ approaches that of the point charge alone; and at the grounded surface and points very far from $\pm m$, $\Phi \to 0$.

An alternative approach in lieu of a formal solution is the image method, which replaces bounding surfaces by appropriate image charges. As an illustration, Fig. 2(a) shows the magnetic charge $\pm m$ in the free space enclosed by the spherical boundary (of radius R) of very high permeability ($\mu \to \infty$, such as iron), where $\pm$ signs designate that the pole is a source or a sink respectively. The interest here is to determine the Φ distribution inside the grounded spherical surface due to the charge m.

In Fig. 2(a) where XYZ is the reference coordinate system, $\bar{m}$ is the image of the charge m and lies along the radial line connecting m. The image charge must be outside the region in which the field is to

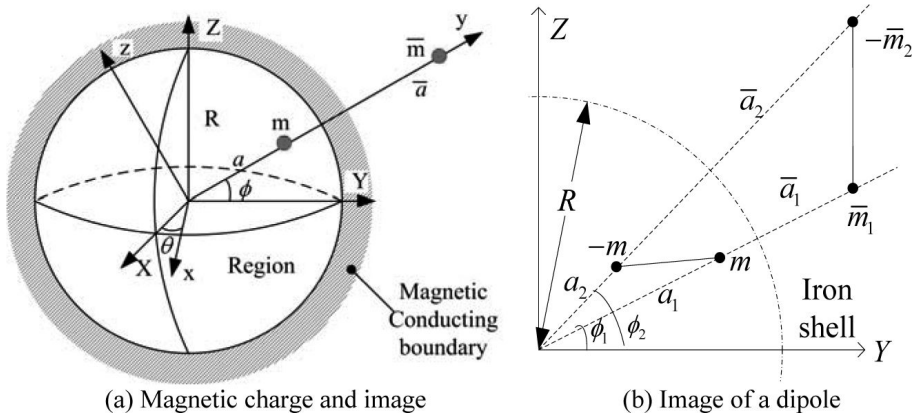

(a) Magnetic charge and image (b) Image of a dipole

Fig. 2. Spherical magnetic boundary.

be determined, the parameters (m, a) and $(\bar{m}, \bar{a})$ are related by (2):

$$\bar{a}/R = -\bar{m}/m = \Lambda \text{ where } \Lambda = R/a \tag{2}$$

To facilitate the discussion, we define a local *xyz* coordinate system (shown in Fig. 2) such that m and $\bar{m}$ are on the y-axis at the vector positions, **a** and $\bar{\mathbf{a}}$, respectively. Any point **x**(x, y, z) can be expressed in spherical coordinates (r, θ, ϕ) with respect to the reference XYZ coordinate system:

$$\mathbf{x}/\left|\mathbf{x}\right| = \begin{bmatrix}\cos\theta\cos\phi & \sin\theta\cos\phi & \sin\phi\end{bmatrix}^T \tag{3}$$

where $\theta = \tan^{-1}(y/x)$; and $\phi = \cos^{-1}(z/\left|\mathbf{x}\right|)$. Due to the symmetry of a sphere, the problem can be reduced to two dimensional (2D) in the yz plane. The potential at point **p**(x,y,z) for $0 \leqslant p \leqslant R$ where $p = |\mathbf{p}|$ is given by

$$\Phi(\mathbf{p}) = \frac{m}{4\pi}\left(\frac{1}{\sqrt{p^2 + a^2 - 2\mathbf{p}\bullet\mathbf{a}}} - \frac{1}{\sqrt{(p/\Lambda)^2 + R^2 - 2\mathbf{p}\bullet\mathbf{a}}}\right) \tag{4}$$

where $a = |\mathbf{a}|$; and $\bar{a} = |\bar{\mathbf{a}}|$. It can be seen from (4) that when $|\mathbf{p}| = R$ (on spherical surface), Φ vanishes. The solution is exactly the same as that between the charge m with the grounded boundary at R.

2.1. Images of a magnetic dipole

Since magnetic poles exist in pairs, we define a dipole as a pair of source m and sink $-m$ separated by a distance d. For the dipole (located at a_1 and a_2), the images of its source and sink are denoted as $\bar{m}_1$ and $-\bar{m}_2$ in Fig. 2(b). Using (2) and (4), the potential at **p** in the free space containing the dipole can be expressed as

$$\Phi(\mathbf{p}) = (m/4\pi)\left[\left(|\mathbf{r}_1|^{-1} - |\bar{\mathbf{r}}_1|^{-1}\Lambda_1\right) - \left(|\mathbf{r}_2|^{-1} - |\bar{\mathbf{r}}_2|^{-1}\Lambda_2\right)\right] \tag{5}$$

where

$$\mathbf{r}_i = \mathbf{p} - \mathbf{a}_i; \quad \bar{\mathbf{r}}_i = \mathbf{p} - \bar{\mathbf{a}}_i \tag{6a,b}$$

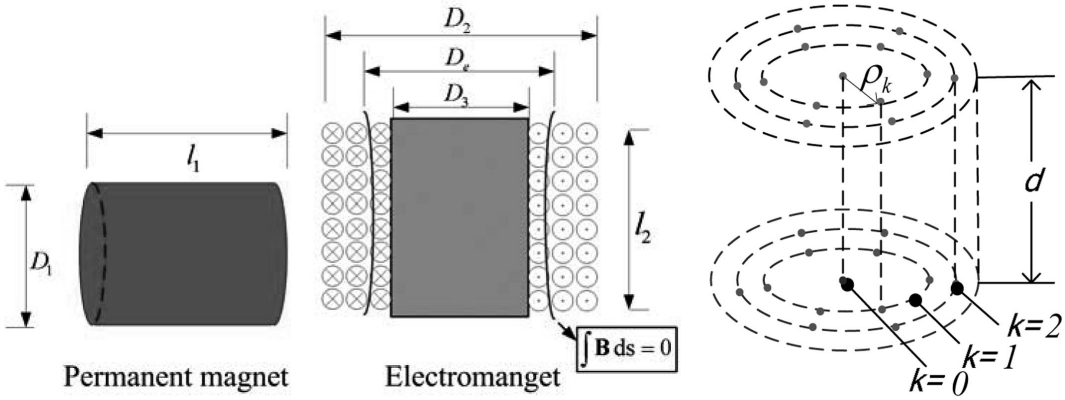

(a) Parameters of PM and EM (b) DMP model

Fig. 3. Parameters of PM and EM and equivalent models.

$$\mathbf{a}_i/\left|\mathbf{a}_i\right| = \bar{\mathbf{a}}_i/\left|\bar{\mathbf{a}}_i\right| = \begin{bmatrix} 0 & \sin\phi_i & \cos\phi_i \end{bmatrix}^T \tag{7}$$

and $i = 1, 2$ denote the source and sink respectively. In general, if $\mathbf{a}_1 \neq \mathbf{a}_2$, $\bar{m}_1 \neq \bar{m}_2$; the images of a dipole do not form another dipole, and do not satisfy the condition for continuous flow, $\nabla \bullet B = 0$. The solution of the image method is invalid in the grounded sphere since the image dipole does not actually exist but the images are rather standing in for the magnetic densities induced on the magnetic boundary.

2.2. Image method for spherical EM actuator

Without loss of generality, we consider in the following discussions PM-based electromagnetic systems which consist of axially magnetized PMs and air-cored EMs. For the purpose of deriving closed-form field solutions to facilitate design and control of PM-based spherical motors, we seek the field solutions outside the physical regions among the PMs, EMs and magnetic boundary. The parameters characterizing the geometries of the PM and EM are defined in Fig. 3(a) and (b) respectively. Using the DMP method [6], we use k circular loops of n equally spaced dipoles (of strength m_k and parallel to the magnetization vector) on the circular loop of radius ρ_k to model the PM or EM as illustrated in Fig. 3. For practical applications, we consider the following cases in spherical coordinates (r, θ, ϕ):

2.2.1. Case 1

The dipole m (with its source and sink located at $\mathbf{x}_{r1}$ and $\mathbf{x}_{r2}$ respectively) is located outside the grounded spherical *rotor* of radius r_r at

$$\left|\bar{\mathbf{x}}_{ri}\right|/r_r = -\bar{m}_{ri}/m = \Lambda_{ri} \text{ where } \Lambda_{ri} = r_r/\left|\mathbf{x}_{ri}\right| \tag{8}$$

and

$$\mathbf{x}_{ri}/\left|\mathbf{x}_{ri}\right| = \bar{\mathbf{x}}_{ri}/\left|\bar{\mathbf{x}}_{ri}\right| = \begin{bmatrix} \cos\theta_i\cos\phi_i & \sin\theta_i\cos\phi_i & \sin\phi_i \end{bmatrix}^T; i = 1, 2$$

2.2.2. Case 2

The dipole m (with its source and sink located at $\mathbf{x}_{s1}$ and $\mathbf{x}_{s2}$ respectively) is located inside the hollow grounded spherical *stator* of radius r_s at

$$\left|\bar{\mathbf{x}}_{sj}\right|/r_s = -\bar{m}_{sj}/m = \Lambda_{sj} \text{ where } \Lambda_{sj} = r_s/\left|\mathbf{x}_{sj}\right| \tag{9}$$

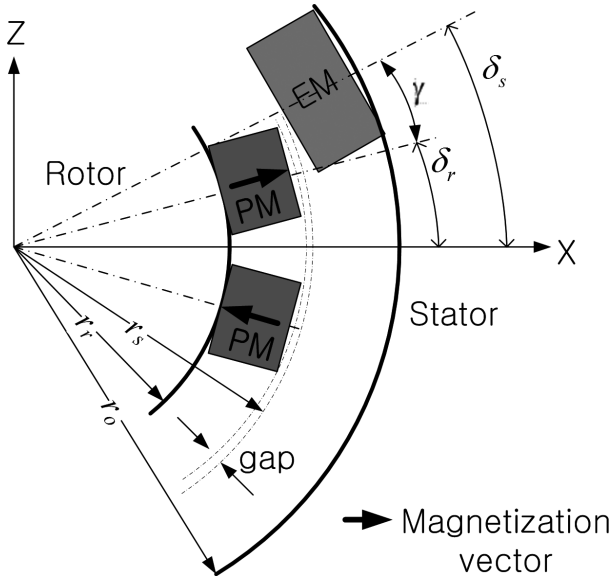

Fig. 4. Electromagnetic system with 2 PM's and 1 EM.

and

$$\mathbf{x}_{sj}/\left|\mathbf{x}_{sj}\right| = \bar{\mathbf{x}}_{sj}/\left|\bar{\mathbf{x}}_{sj}\right| = \begin{bmatrix}\cos\theta_j\cos\phi_j & \sin\theta_j\cos\phi_j & \sin\phi_j\end{bmatrix}^T; j = 1,2$$

2.2.3. Case 3

The dipole m is in-between the grounded spherical *rotor and stator*, which are concentric. Each of the charges (source or sink) has two images located such that $\theta_i = \theta_j = \theta$ and $\phi_i = \phi_j = \phi$:

$$\bar{\mathbf{x}}_{ri}/\left|\bar{\mathbf{x}}_{ri}\right| = \bar{\mathbf{x}}_{sj}/\left|\bar{\mathbf{x}}_{sj}\right| = \begin{bmatrix}\cos\theta\cos\phi & \sin\theta\cos\phi & \sin\phi\end{bmatrix}^T \text{ where } i,j = 1,2 \tag{10}$$

Case 3 is essentially a linear combination of Cases 1 and 2 since the Laplace equation is linear. With the specified magnetic dipole and boundary, the images of the source and sink can be calculated from (8), (9) or (10), Φ and hence **H** in the free space can be found from (5) and (1) respectively.

3. Illustrative examples

The example considered here is an electromagnetic system consisting of two axially magnetized PM on the spherical rotor, and an air-cored EM on the inside surface of the hollow spherical stator. As shown in Fig. 4 where characteristic dimensions are defined, the two rotor-PM poles are identical but their magnetization vectors are in opposite directions. In Fig. 4, δ_r and δ_s define the magnetization vectors of the rotor-PM and stator-EM in their respective body coordinate frames. The interest here is to investigate the effects of the iron boundaries on the magnetic field distribution (in the region between the rotor and stator surfaces) and torques acting on the rotor (as a function of the separation angle γ). For this, we compare four different design configurations (DC):

DC1: Rotor and stator are non-magnetic boundaries.

DC2: Only the rotor is a magnetically conducting sphere.

Table 1A
Comparisons of design parameters*

Spheres	Design A	Design B
r_r, r_s, g	25.4, 64.3, 0.76	38.1, 64.3, 0.76
PM: l_1, D_1, M_o	12.7, 12.7, 1.34T	12.7, 19.05, 1.34T
EM: l_2, D_2, D_3	25.4, 19.05, 9.525	19.05, 20.32, 7.62
N, I	1040, 4A	1040, 4A

*Geometrical dimensions are in mm; N = # of turns

Table 1B
DMP parameters of PM

Parameters	Design A ($n = 6, k = 1$)	Design B ($n = 6, k = 1$)
d/l_1	0.514	0.3028
$2\rho_o/D_1$, m_o (μAm)	0, -22.9	0, -47.2
$2\rho_1/D_1$, m_1 (μAm)	0.5, 61.8	0.5, 180.8
% error	3.3	3.6

Table 1C
Equivalent DMP parameters of EMs

Parameters	Design A ($n = 6, k = 1$)	Design B ($n = 6, k = 1$)
$d/l_2, D_e$	0.9165, 18.59	0.9501, 18.35
$2\rho_o/D_e, m_o$ (nAm)	0, 14.8	0, 5.6
$2\rho_1/D_e, m_1$ (nAm)	0.5, 108.3	0.5, 54.8
% error	5.7	6.73

D_e: switching diameter

DC3: Only the stator is a magnetic conducting boundary.
DC4: Both the rotor and the stator are magnetic boundaries.

Once the magnetic field is known, its effects on the torque acting on the rotor can be investigated by comparing two design geometries; Designs A and B. The (PM and EM) geometries, which are based on the spherical motor in [14], and their corresponding DMP models are given in Tables 1A-C. Table 1A compares the two design geometries, where the differences are highlighted in bold; and g is the radial air-gap between the air-cored EM and rotor PMs. The values characterized the DMP models of the PM and EM are given in Tables 1B and 1C respectively, where the % error is DMP modeling error defined along the PM magnetization axis:

$$\%\text{error} = 100 \times \frac{\int\limits_z |\Phi(z) - \Phi_A(z)|\, dz}{\int\limits_z |\Phi_A(z)|\, dz}$$

The corresponding images (location and strength) reflecting the source and sink of each dipole on the spherical boundaries can be derived from (5) with (8), (9) or (10).

3.1. No current flowing through the air-core EM

The simulated magnetic fields are given in Figs 5 and 6, where the bold solid circles indicate the spherical boundaries (black for the rotor and red for the stator). Figure 5 shows the magnetic field in Design A due to the PM pair between two concentric grounded spheres. To visually illustrate the image method, we graph the effects of images of the dipoles in the grounded spheres. It must be emphasized

Table 2
% Increase in maximum torque relative to DC1

Designs	DC2 (iron rotor)	DC3 (iron stator)	DC4 (both)
Design A	3.2 %	6.0 %	9.2 %
Design B	8.68 %	15.15 %	23.73 %

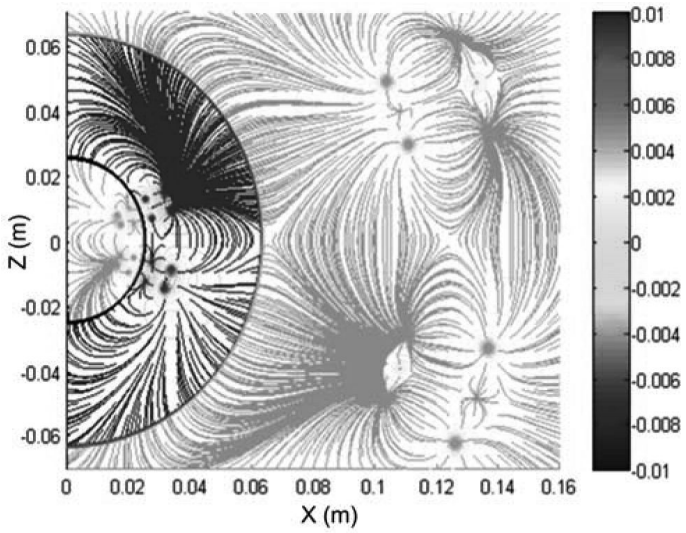

Fig. 5. PM Pair between two magnetic surfaces (Unit of colormap: Tesla (T)).

that the field distributions calculated using the image method are valid only in the free space between the spheres, and are invalid in the magnetically ground spheres where Φ and $\mathbf{H}$ are zero in iron ($\mu \rightarrow \infty$) and are veiled in Fig. 6.

Figure 6(a) shows the magnetic field of the DC1 (with no grounded boundaries) which provides a basis for comparison. The effects of the iron rotor and stator boundaries on the magnetic field are compared in Figs 6(b) and 6(c) respectively. As expected, the magnetic field is perpendicular to grounded spherical surface ($\Phi = 0$). Similarly, the combined effect of both the iron rotor and stator boundaries on the magnetically field is graphically displayed in Fig. 6(d).

3.2. Effects of pole design with iron boundary on torque

Using the DMP method with multi-dipoles for the PM and their images, the magnetic field in the air space between the two conducting surfaces and hence, the torque can be computed from the Lorentz force Eq. (A.1) or the forces between magnetic charges (A.3). Alternatively, if the total field (including both PM and EM) is known, the force on a body can also be computed from the surface integration in term of Maxwell stress tensor (A.2). For completeness, the equations for computing the magnetic torque are given in Appendix A.

We examine the effects of iron boundaries on the magnetic torque by comparing the four design configurations for a given stator radius r_s, each with two different design geometries. In each design, the computed torques for the four DC's are plotted as a function of the separation angle γ (between the magnetization axes of the PM and EM) in Fig. 7. The % increases in the maximum torques relative to DC1 are compared in Table 2.

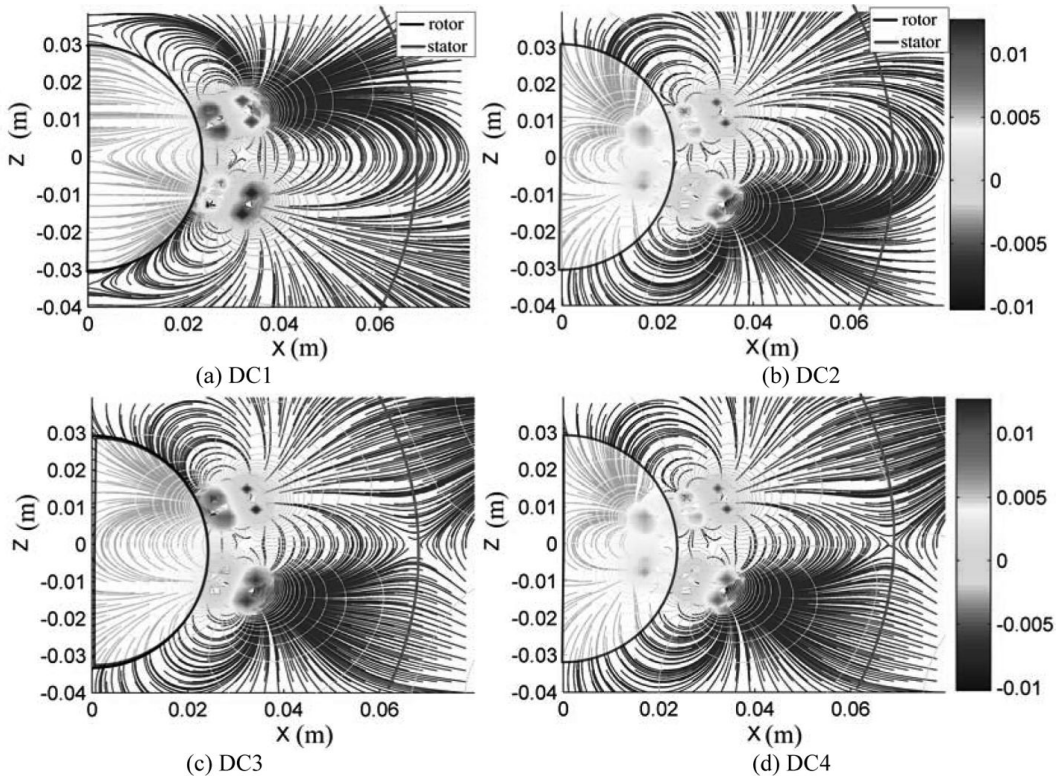

Fig. 6. Effect of boundaries on magnetic field (Unit of colormap: Tesla (T)).

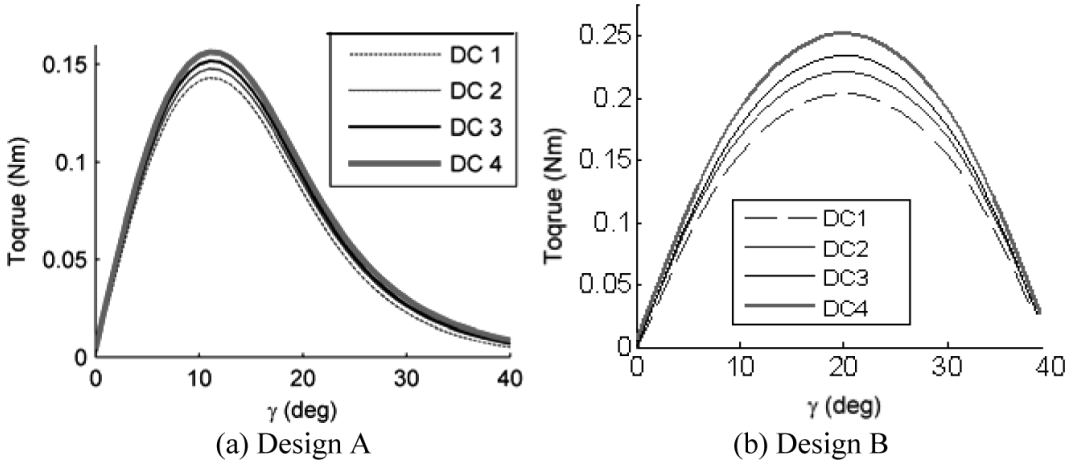

Fig. 7. Effect of iron boundaries on torque.

In Design A, the combined rotor/stator irons (DC4) contribute to 9.2% increase in the maximum torque; two-thirds are from the iron stator shell and the remainder is from the iron rotor. The results are consistent with the predicted magnetic field distributions and can be explained with the aid of Fig. 6 as follows. DC4 has shortest magnetic flux paths as they enter perpendicularly into grounded boundary. The

shorter flux path in DC4 (relative to DC1) results in higher magnetic field intensity and thus larger force on the stator EM. In DC1, the magnetic flux paths between two EMs in the r_s region are much longer than that between two PMs in the r_r region; this suggests that the iron stator plays a more significant role in shortening the path lines than the iron rotor.

4. Simulation results and discussion

In this section, we present and discuss the following torque results computed using the DMP-Image method:

– Numerical validation and torque computation time
– The DMP-Image method for analyzing designs of a spherical wheel motor (SWM).

In the following design examples, both the rotor PM and stator EM are on iron conductors. All computation was performed on a Windows-based PC (dual core processor 2.21 Ghz CPU and 1GB memory).

4.1. Numerical validation

To validate the torque computation using the magnetic fields from the DMP-Image, the computed torque for the electromagnetic system in Fig. 7(a) [13] where the geometries of the diagonally symmetric PM and EM pole-pairs are based on Design A in Table 1. In Fig. 8(a), the rotor with a pair of PMs rotates with respect to the stator with two EMs on the same plane. In this study, the torque about the axis perpendicular to this plane is computed as a function of the separation angle γ and compared against solutions numerically obtained using ANSYS (a commercial FE analysis package) in Fig. 8(b).

4.1.1. ANSYS model

The ANSYS FE model uses cylindrical iron boundaries for simplicity due to the symmetry. The procedure for computing the electromagnetic torque using ANSYS can be found in [15]. In ANSYS, the iron boundary was modeled using the eight-node SOLID96 elements ($\mu_r = 1000$ where μ_r is the relative permeability); the free space air volume was modeled using four-node INFIN47 elements; and the air-cored stator coil as SOURCE36 elements. For the PM, $\mu = B_r/H_c$ where B_r and H_c are the residual magnetization and the magnitude of coercive force vector respectively. In this computation, $H_c = 795{,}770$ A/m and $B_r = 1.34$T. With the total magnetic flux density from ANSYS, the torque acting on the rotor is computed using (A.2) where Γ is a circular boundary enclosing the rotor including the PM.

4.1.2. Image method with DMP model (DMP-image)

For the image method, the PM and EM pole-pairs are replaced by their respective DMP models, and their images are found following the procedure as discussed in Section 3. The resulting magnetic torque on the rotor can be computed using one of the three methods outlined in the appendix.

Using the DMP-Image, the Maxwell stress tensor (A.2) and the magnetic charge equation (A.3) yield identical torque solutions, which agree (within 5% difference) with the ANSYS results shown in Fig. 8(d). Due to symmetry, there should be no torque generated when the separation angle γ is zero, which the PM and EM pole-pairs are aligned. The discrepancy (offset at $\gamma = 0$) in ANSYS could be because of the automatically generated FE mesh; this suggests that the quality of mesh could significantly affect the accuracy of the FE analysis. In addition, the DMP-Image with Lorentz force equation (A.1) took only 17 seconds to compute the torque curve while ANSYS requires 24.67 minutes to compute the 13 data. Note that (A.3) is in closed-form requiring relatively negligible computation time.

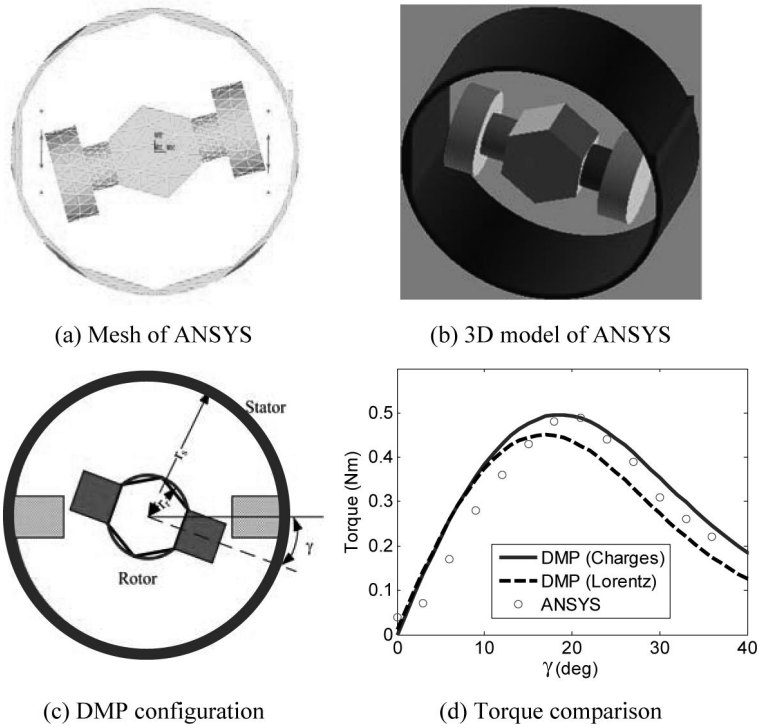

(a) Mesh of ANSYS (b) 3D model of ANSYS

(c) DMP configuration (d) Torque comparison

Fig. 8. Comparisons of computed torques (Computational time: ANSYS = 1,480 seconds. DMP = 17 seconds).

4.2. Effects of iron boundaries on the SWM design

We illustrate the use of the DMP-Image for analyzing the magnetic torque of a spherical wheel motor (SWM) [15]. Unlike a variable-reluctance spherical motor (VRSM) [7] where the rotor PM and stator EM are placed on locations following the vertices of a regular polygon, the PM and EM of a SWM are equally spaced on layers of circular planes with their radial magnetization axes passing through the motor center. The PM and EM are grouped in pairs; and every two PM or EM pole-pairs form a plane providing symmetric forces electro-mechanically. The magnetization axes of the m_r PM pole-pairs are given in rotor coordinates (x, y, z) by Eq. (11):

$$\mathbf{r}_i = (-1)^{i-1} \begin{bmatrix} \cos\delta_r \cos\theta_{ri} & \cos\delta_r \sin\theta_{ri} & \sin\delta_r \end{bmatrix}^T \tag{11}$$

where $\theta_{ri} = (i-1)\theta_r$; and $i = 1, 2, \ldots, m_r$. Similarly, the m_s EM pole-pairs in the stator frame (XYZ) are given by Eq. (12):

$$\mathbf{s}_j = \begin{bmatrix} \cos\delta_s \cos\theta_{sj} & \cos\delta_s \sin\theta_{sj} & \sin\delta_s \end{bmatrix}^T \tag{12}$$

where $\theta_{sj} = (j-1)\theta_s$; and $j = 1, 2, \ldots, m_s$. Unlike m_s which may be odd or even, m_r is always an even number.

4.2.1. Torque – Current relationship of a SWM

The resultant torque of the spherical motor with linear magnetic properties has the following form:

$$\mathbf{T} = \begin{bmatrix} T_X & T_Y & T_Z \end{bmatrix}^T = [\mathbf{K}]\,\mathbf{u} \tag{13}$$

Table 3A
Geometries of the two SWM designs

Parameters*	SWM 1	SWM 2
r_o, r_s, r_r, gap	76.2, 57, 38.5, 0.5	76.2, 48.3, 56.6, 0.5
$\delta_{s'}$, δ_r (°)	26°, 20°	18°, 25°
D_1, ℓ_1; $M_\circ$	25.4, 12.7; 1.34T	31.8, 12.7; 1.34T
D_2, D_3 , ℓ_2; N	19.05, 6,12.7; 1040	25.4, 6, 12.7; 1040
m_s, m_r	10, 8	8, 10

* Dimensions are in mm.

Table 3B
DMP parameters of PM and EM

Design	PM	EM
SWM 1	$k = 2$, $n = 6$; $d/l1 = 0.3100$	k= 2, $n = 6$; $d/l_2 = 0.5833$, $D_e = 15.82$
	m_k: 139.8/9.4/354.7	m_k: 0.1471/0.0105/0.4536
SWM 2	$k = 2$, $n = 6$; $d/l_1 = 0.2984$	$k = 2$, $n = 10$; $d/l = 0.3163$, $D_e = 19.95$
	m_k: 159.2/ 41.0/ 555.5	m_k: 1.06/0.0775/3.031

D_e: switching diameter; m_k: $m_o/m_1/m_2$ in μAm

where

$$\mathbf{K}\left(\in R^{3\times m_s}\right)=\left[K_1\cdots K_j\cdots K_{m_s}\right];K_j=\begin{cases}-\sum_{i=1}^{m_r}\left[\hat{f}(\gamma)\Big|_{\gamma=\gamma_{ji}}\frac{\mathbf{s}_j\times\mathbf{r}_i}{|\mathbf{s}_j\times\mathbf{r}_i|}\right] & \text{if } \mathbf{s}_j\times\mathbf{r}_i\neq 0\\ 0 \quad \text{if } \mathbf{s}_j\times\mathbf{r}_i=0\end{cases}; \text{(14a,b)}$$

and

$$\mathbf{u}=\left[u_1\cdots u_j\cdots u_{m_s}\right]^T \tag{15}$$

K_j is the torque characteristic vector contributed by the j^{th} EM. $\hat{f}(\gamma)$ is a curve-fit function of the torque from Fig. 8(d) as a separation angle γ between a PM pole-pair and an EM pole-pair $\gamma_{ji} = \cos^{-1}\left(\mathbf{s}_j \bullet \mathbf{r}_i\right)/\left(|\mathbf{s}_j|\,|\mathbf{r}_i|\right)$. **u** is current input vector.

Since the SWM has more current inputs than the mechanical DOF, the actual current input vector u for a given torque is found by minimizing the input energy consumption subject to the desired torque constraint (13). Provided that the input currents are kept within limits, the optimal **u** can be solved using Lagrange multipliers. The optimal solution can be written in closed form [7]:

$$\mathbf{u}=[\mathbf{K}]^T\left([\mathbf{K}]\,[\mathbf{K}]^T\right)^{-1}\mathbf{T} \tag{16}$$

4.2.2. Application example

As an illustration, we compare two different designs (denoted here as SWM1 and SWM2 in Fig. 9) for the same r_o of 76.2 mm in Table 3 (at same size). Unlike the SWM1 [16], the SWM2 has 10 rotor PM pole-pairs mounted on the internal surface of the hollow hemi-sphere and 8 EM pole-pairs are on the external surface of the spherical stator. Specifically, the interest here is to determine the current inputs required to provide a specified torque of T = [0 1 0]^T Nm. As shown in Fig. 9, due to symmetry, the current inputs are applied as follows:

SWM1: $u_2 = u_{10}$, $u_3 = u_9$, $u_4 = u_8$, $u_5 = u_7$

SWM2: $u_2 = u_8$, $u_3 = u_7$, $u_4 = u_6$

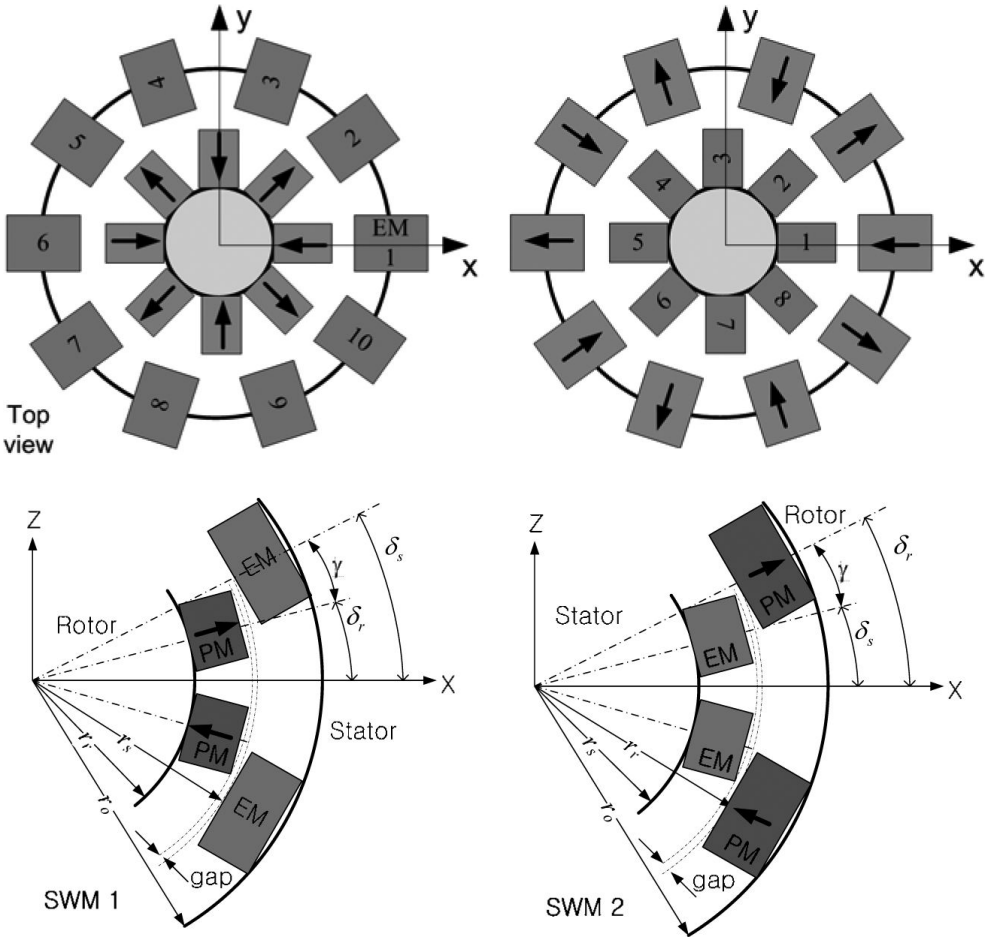

Fig. 9. Schematics illustrating SWM 1 and SWM2.

Figures 10 and 11 compare the current inputs and its norm defined as $J = \mathbf{u}^T\mathbf{u}$. For the same coil resistances, the maximum current and the total energy input required by SWM 2 are significantly lower than that required by SWM 1. While (A.2) and (A.3) yield identical results, the average time for computing the applied torque at a specified orientation using the magnetic charge method requires only 0.25 seconds. The Maxwell stress tensor method, however, would require 220 seconds for the same calculation.

5. Conclusion

We have shown how the DMP-Image method can be used to analyze a class of spherical motors where PMs and/or EMs are in the presence of magnetically grounded conducting boundary. The DMP-Image method, which solves the magnetic fields in closed form, has been validated by comparing the torques calculated using three different methods (Lorentz, Maxwell and magnetic charges) against the numerical results computed using FEM with Maxwell stress tensor. While the comparison agrees to within 5% in maximum torque, the DMP-Image method requires less than 1% of the FEM computation time. A

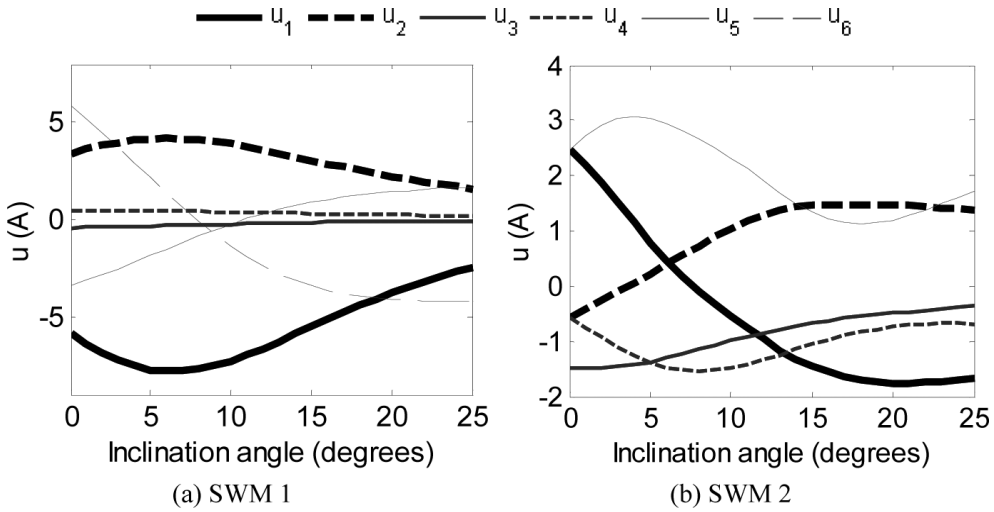

(a) SWM 1 (b) SWM 2

Fig. 10. Currents inputs.

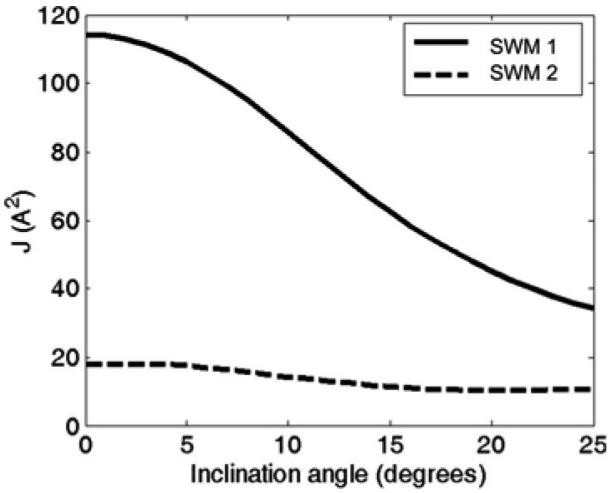

Fig. 11. Comparison of total energy input.

relatively complete formulation has been presented for solving the magnetic field of a spherical motor with three different cases of magnetically grounded surfaces. As an illustration of practical applications, we demonstrate the effectiveness of using the DMP-Image solutions for analyzing the design of a magnetically linear spherical wheel motor.

Appendix A. Torque calculation

Three methods for computing the magnetic torque are given as follows:
Lorentz force equation:

$$\mathbf{T} = -\int \mathbf{p} \times \mathbf{B} \times (Id\bar{\ell}\,) \text{ where } I = -\iint \mathbf{J} \bullet d\mathbf{S} \tag{A.1}$$

where $\bar{\ell}$ is the normalized current direction vector. In (A.1), the current density vector **J** is directly used in the calculation and thus, it involves only modeling the **B**-fields of the permanent magnets.

Maxwell stress tensor:

Alternatively, if the total B field (including both PM and EM) is known, the force on a body can also be computed from the surface integration in term of Maxwell stress tensor

$$\mathbf{T} = \frac{1}{\mu_0} \int_{\Gamma} \mathbf{p} \times \left(\mathbf{B}(\mathbf{B} \bullet \mathbf{n}) - \frac{1}{2} B^2 \mathbf{n} \right) d\Gamma \tag{A.2}$$

where Γ is an arbitrary boundary enclosing the body of interest; and n is the normal of the material interface.

Force on magnetic charges [17]

Figure A1 shows a dipole in the magnetic field, where HR+ and HR- are the magnetic field intensities acting on the magnetic source and sink of the dipole respectively; and R_+ and R_- are the corresponding distances from a field point. The force **F** on the magnetic dipole can be written (in analogy to that on the force on a stationary electric charge by the Lorentz law) as

$$\mathbf{F} = \mu_o m \left[\mathbf{H}_{R+} - \mathbf{H}_{R-} \right] \tag{A.3}$$

Similarly, the torque on a dipole

$$\mathbf{T} = \mathbf{R}_+ \times \mathbf{F}_+ + \mathbf{R}_- \times \mathbf{F}_- = \mu_o m \left[\mathbf{R}_+ \times \mathbf{H}_{R+} - \mathbf{R}_- \times \mathbf{H}_{R-} \right] \tag{A.4}$$

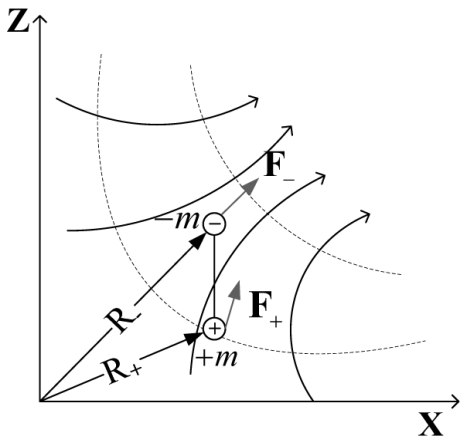

Fig. A1. Force on a dipole in the magnetic field.

References

[1] S. Sudo, K. Tsuyuki, T. Matsumoto, M. Yoshikawa, M. Watanabe and T. Honda, Biomimetic study of diving beetle robot propelled by alternating magnetic field, *Int J Applied Electro and Mech* **25** (2007), 601–606.

[2] E. Stump and V. Kumar, Workspaces of Cable-Actuated Parallel Manipulators, *ASME, J of Mechanical Design* **128** (2006), 159–167.

[3] Zhu, Yu-Wu Kim, Do-Sun; Moon, Ji-Woo and Cho, Yun-Hyun, Analysis of permanent magnet linear synchronous motor for advanced control, *Int J Applied Electro and Mech* **28** (2008), 283–289.

[4] K.-M. Lee, Q. Li and H. Son, Effects of numerical formulation on magnetic field computation using meshless methods, *IEEE Trans.on Magnetics* **42** (2006), 2164–2171.
[5] H. Ghoizad, M. Mirsalim, M. Mirzayee and W. Cheng, Coupled magnetic equivalent circuits and the analytical solution in the air-gap of squirrel cage induction machines, *Int J Applied Electro and Mech* **25** (2007), 749–754.
[6] K.-M. Lee and H. Son, Distributed multipole model for design of permanent-magnet-based actuators, *IEEE Trans on Magnetics* **43** (2007), 3904–3913.
[7] H. Son and K.-M. Lee, Distributed Multi-Pole Models for Design and Control of PM Actuators and Sensors, *IEEE Trans on Mechatronics* **13** (2008), 228–238.
[8] L. Yan, I.-Ming Chen, G. Yang and K.-M. Lee, Analytical and Experimental Investigation on the Magnetic Field and Torque of a Permanent Magnet Spherical Actuator, *IEEE Trans. on Mechatronics* **11** (2006), 409–419.
[9] K. Lee and K. Park, Modeling eddy currents with boundary conditions by using Coulomb's law and the method of images, *IEEE Trans on Magnetics* **38** (2002), 1333–1340.
[10] I. Dufour and D. Placko, Original approach to Eddy current problems through a complex electrical image concept, *IEEE Trans on Magnetics* **32** (1996), 348–365.
[11] Y. Saito, K. Takashi and S. Hayano, Finite element solution of unbounded magnetic field problem containing ferromagnetic materials, *IEEE Trans on Magnetics* **24** (1988), 2946–2948.
[12] G. Xiong and S.A. Nasar, Analysis of fields and forces in a permanent magnet linear synchronous machine based on the concept of magnetic charge, *IEEE Trans on Magnetics* **25** (1989), 2713–2719.
[13] L. Kapjin and P. Kyihwan, Modeling eddy currents with boundary conditions by using Coulomb's law and the method of images, *IEEE Trans on Magnetics* **38** (2002), 1333–1340.
[14] K.-M. Lee, R.A. Sosseh and Z. Wei, Effects of the Torque Model on the Control of a VR Spherical Motor, *IFAC J of Control Engineering Practice* **12/11** (2004), 1437–1449.
[15] K.-M. Lee, H. Son and J. Joni, Concept Development and Design of a Spherical Wheel Motor (SWM), *Proc of ICRA* (2005), 3652–3657.
[16] K.-M. Lee, J. Joni and H. Son, Design Method for Prototyping a Cost-Effective Variable-Reluctance Spherical Motor (VRSM) *Proc IEEE Conference on Robotics, Automation and Mechatronics Singapore* **1** (2004), 542–547.
[17] D.B.H. Tellegen, Magnetic-dipole models, *Am J Phys* **30** (1962), 650–652.

Copyright of International Journal of Applied Electromagnetics & Mechanics is the property of IOS Press and its content may not be copied or emailed to multiple sites or posted to a listserv without the copyright holder's express written permission. However, users may print, download, or email articles for individual use.